catalysts

MDPI

Article

SnO_2 Quantum Dot-Decorated g-C_3N_4 Ultrathin Nanosheets: A Dual-Function Photocatalyst for Pollutant Degradation and Hydrogen Evolution

Surya Veerendra Prabhakar Vattikuti [1,*], Hemanth P. K. Sudhani [2], Mohamed A. Habila [3], P. Rosaiah [4] and Jaesool Shim [1,*]

[1] School of Mechanical Engineering, College of Engineering, Yeungnam University, Gyeongsan 38541, Republic of Korea
[2] Department of Biotechnology, SRM Institute of Science and Technology (SRMIST), Tiruchirappalli Campus, Tiruchirappalli 621105, Tamil Nadu, India; sudhanip@srmist.edu.in
[3] Department of Chemistry, College of Science, King Saud University, P.O. Box 2455, Riyadh 11451, Saudi Arabia
[4] Department of Physics, Saveetha School of Engineering, Saveetha Institute of Medical and Technical Sciences (SIMATS), Thandalam, Chennai 602105, Tamil Nadu, India
* Correspondence: vsvprabu@gmail.com (S.V.P.V.); jshim@ynu.ac.kr (J.S.)

Abstract: The development of advanced functional composite materials for degrading industrial pollutants and achieving photocatalytic hydrogen (H_2) production using abundant solar energy is pivotal in new and renewable energy research. This study presents the synthesis of a nanostructure comprising SnO_2 quantum dots (QDs) randomly dispersed on the surface of graphitic carbon nitride (C_3N_4) nanosheets (Sn-C_3N_4), achieved through the thermal decomposition of melamine and a tin precursor. The synthesized materials were extensively characterized using various analytical techniques, with HRTEM analysis confirming the strong interaction between SnO_2 QDs and C_3N_4. The influence of SnO_2 QDs on the nanocomposite's photocatalytic performance was evaluated, particularly regarding H_2 production and the degradation of crystal violet (CV) dye under simulated solar-light irradiation. The SnO_2-loaded C_3N_4 nanostructure exhibited a marked enhancement in photocatalytic activity, attributed to the synergistic effects of the quantum-sized SnO_2 nanoparticles. The optimized photocatalyst, 3-Sn-C_3N_4, demonstrated superior photocatalytic efficiency, achieving 95% degradation of CV dye within 45 min under simulated sunlight, significantly outperforming bare C_3N_4. Furthermore, the 3-Sn-C_3N_4 nanostructure attained the highest H_2 yield of 1305.4 µmol/h/g, a 4.6-fold increase compared with bare C_3N_4 (281 µmol/h/g). Enhanced photocatalytic performance was corroborated by photocurrent and EIS studies, which highlighted reduced charge carrier recombination as a critical factor in the improved activity. The underlying photocatalytic mechanisms were also examined.

Keywords: quantum dots; photocatalysts; dye degradation; hydrogen production; 2D materials

Citation: Vattikuti, S.V.P.; Sudhani, H.P.K.; Habila, M.A.; Rosaiah, P.; Shim, J. SnO_2 Quantum Dot-Decorated g-C_3N_4 Ultrathin Nanosheets: A Dual-Function Photocatalyst for Pollutant Degradation and Hydrogen Evolution. *Catalysts* **2024**, *14*, 824. https://doi.org/10.3390/catal14110824

Academic Editor: Jean-François Lamonier

Received: 19 October 2024
Revised: 12 November 2024
Accepted: 13 November 2024
Published: 15 November 2024

1. Introduction

As society progresses, there is growing emphasis on resource conservation and environmental protection. The pursuit of green and renewable energy has become a vital strategy for addressing energy shortages and promoting ecofriendly solutions. Photocatalysis has emerged as a promising green technology for tackling two critical global challenges: environmental pollution and sustainable energy production. Specifically, photocatalytic water splitting to produce hydrogen (H_2) offers a clean energy solution by harnessing sunlight to generate renewable fuel. Simultaneously, photocatalysis can play a crucial role in degrading harmful pollutants in water, contributing to environmental remediation [1,2]. Dual-function photocatalysts, which combine both of these functions in a single material,

hold the potential to address pollution and energy demands simultaneously [3,4]. To date, a wide variety of photocatalysts have been investigated for photocatalytic hydrogen evolution applications, including metal oxides, C_3N_4, and metal sulfides. Among these materials, C_3N_4 has garnered considerable interest due to its moderate band gap, which enables visible light absorption, as well as its notable thermal and chemical stability [5]. However, the relatively low inherent photocatalytic efficiency of g-C_3N_4 constrains its practical applications across a broader range of fields.

To overcome this limitation, several strategies have been proposed, such as modifying the electronic structure, enhancing electron transfer rates, expanding visible light absorption, and forming heterostructures or nanocomposites [6]. Techniques like element doping, heterojunction formation, co-catalyst addition, and microstructural modifications have been widely adopted to optimize the electronic properties of C_3N_4 [7]. Extensive research has demonstrated the effectiveness of these approaches in improving photocatalytic performance.

Fareed et al. [8] reported a significant improvement in photocatalytic performance using a C_3N_4/SnS_2 nanostructure. Their result demonstrated that this composite material achieved 90% degradation of MB dye within just 90 min under solar irradiation. This high degradation efficiency was attributed to the Type II heterojunction mechanism in the C_3N_4/SnS_2 system, which facilitated efficient charge transfer between the two components. In this Type II heterostructure, the conduction band of SnS_2 is positioned below that of C_3N_4, allowing the electrons to flow directionally from C_3N_4 to SnS_2. Concurrently, holes are transferred in the opposite direction, promoting effective charge separation and minimizing charge carrier recombination—a key factor that typically limits photocatalytic efficiency. The reduced recombination of charge carriers not only accelerates the degradation of organic pollutants but also shows promise for enhancing other photocatalytic applications, including H_2 generation. In a study by Alsalme [9], a C_3N_4-based composite was further optimized by incorporating 15 wt% SnS_2, resulting in a notable improvement in photocatalytic performance. This C_3N_4/SnS_2 nanostructure achieved 98% degradation of RhB dye within 120 min under solar irradiation, whereas bare C_3N_4 only managed to degrade 35% of the RhB dye in the same period. This limitation in bare C_3N_4 is largely due to its poor light absorption and rapid recombination of electron–hole pairs caused by uncontrolled electrostatic interactions. Alsalme's study underscores the effectiveness of tuning photocatalysts' composition and structure to enhance performance. The dramatic increase in RhB dye degradation highlights the potential of combining C_3N_4 with metal sulfides like SnS_2 as a strategy to overcome the limitations of single-component photocatalysts. This approach opens avenues for developing more efficient multifunctional materials for environmental remediation and solar energy applications.

Lu et al. [10] reported a significant enhancement in photocatalytic H_2 production using a novel carbon dot-loaded black-C_3N_4 nanostructure. This composite demonstrated impressive photothermal-assisted photocatalytic activity, achieving a H_2 yield of 3.4 mmol/g/h, far surpassing conventional C_3N_4-based materials. This superior performance was attributed to several key factors that set the carbon dot-loaded black-C_3N_4 apart from its unmodified counterpart. The introduction of carbon dots not only enhances the hydrophilicity of the black-C_3N_4 nanostructure, promoting better interaction with water molecules—which is critical for efficient photocatalytic water splitting—but also contributes to improved charge transfer and increased surface area. This combination offers a promising approach to overcoming the limitations of traditional photocatalysts, making this material a strong candidate for future renewable energy applications.

Metal QDs have attracted considerable attention in photocatalytic applications due to their unique quantum confinement effects, which confer distinct optical and electronic properties. These effects enable QDs to play a pivotal role in enhancing photocatalytic processes. It is well established that integrating QDs with semiconductor materials can substantially improve the efficiency of both photocatalytic pollutant degradation and H_2 production from aqueous solutions [11,12]. In such systems, QDs act as efficient electron

acceptors, facilitating charge separation by capturing photogenerated electrons from the semiconductor. This enhanced electron transfer is essential for driving photocatalytic reactions, as it helps suppress charge recombination—a key factor limiting the efficiency of bare semiconductor photocatalysts. By acting as electron sinks, QDs not only extend the lifetime of charge carriers but also promote the formation of reactive radicals, which play a critical role in degrading water pollutants. Additionally, captured electrons can be directed toward the H_2 evolution centers, further boosting H_2 production efficiency. Thus, the inclusion of QDs in photocatalytic systems offers a dual benefit: improving pollutant degradation through radical generation and enhancing H_2 production by optimizing the charge transfer mechanisms [12]. These properties make QD-supported semiconductor materials highly promising for various applications, including environmental remediation and sustainable energy production. Continued exploration of QD–semiconductor composites is expected to yield more efficient, versatile photocatalytic materials capable of addressing critical environmental and energy challenges. In recent studies, Bhattacharjee et al. [13] demonstrated the exceptional photocatalytic performance of a SnO_2 QDs/C_3N_4/biochar nanostructure synthesized via a one-pot pyrolysis method. This composite material achieved impressive degradation efficiencies, with up to 96% degradation of Rose Bengal in 80 min and 95% degradation of MB in 120 min under irradiation. The high photocatalytic activity was attributed to the advanced oxidation process enabled by the synergistic effects of SnO_2 QDs, C_3N_4, and biochar components. Khan et al. [14] reported a significant enhancement in photocatalytic activity using an ultrasound-assisted coprecipitated ZnS QDs/C_3N_4 nanostructure, which achieved up to 98% degradation of RhB within just 54 min, with a rate constant of 0.077/min. The outstanding photocatalytic efficiency can be explained by the quantum confinement effects of ZnS QDs, which were dispersed on the surface of C_3N_4, dramatically improving the system's overall performance. The incorporation of ZnS QDs onto C_3N_4 nanosheets enhanced light absorption and facilitated efficient electron–hole separation. The quantum effect of ZnS QDs increased the number of reactive centers on the nanostructure's surface, accelerating the degradation of organic pollutants like RhB. Additionally, ZnS QDs acted as electron reservoirs, reducing the recombination rate of photoexcited electrons and holes—a primary limitation of pure C_3N_4. Despite these advancements, challenges remain, particularly in developing efficient synthesis methods that ensure well-matched interfaces and precise band structure alignment within heterostructures. These factors are crucial for optimizing photoinduced charge separation and transfer, which are essential for maximizing photocatalytic efficiency.

In this study, we developed a SnO_2 QDs/C_3N_4 nanostructure through a straightforward single-step pyrolysis of a tin (Sn) precursor and melamine. This nanocomposite was utilized as an effective photocatalyst for both CV dye decolorization and H_2 production under solar light irradiation. Varied concentrations of SnO_2 QDs were used to assess its effect on photocatalytic performance, specifically regarding dye degradation and H_2 generation. Moreover, the underlying photocatalytic mechanisms driving these processes were thoroughly examined and discussed. The results revealed that the optimized 3-Sn-C_3N_4 nanostructure exhibited significantly enhanced photocatalytic activity compared with bare C_3N_4, primarily attributed to the synergistic interaction between the SnO_2 QDs and C_3N_4 nanosheets. The QDs not only facilitated more efficient charge separation, reducing electron–hole recombination, but also contributed to an increased surface area, providing additional active sites for photocatalytic reactions. These combined factors led to a significant rise in the degradation rate of CV dye and a notable improvement in H_2 production efficiency. This work underscores the potential of SnO_2 QD-C_3N_4 nanostructures as versatile and highly effective photocatalysts, with promising applications in environmental remediation and renewable energy production. The findings also highlight the importance of nanostructure design and material optimization in achieving superior photocatalytic performance under solar light irradiation.

2. Results and Discussion

The XRD patterns of bare C_3N_4 and the Sn-C_3N_4 nanostructures (1-Sn-C_3N_4, 2-Sn-C_3N_4, and 3-Sn-C_3N_4) are shown in Figure 1. For C_3N_4, a prominent peak at 2θ = 27.76° corresponds to the (002) crystal plane, consistent with previous reports [15,16]. The diffraction peaks observed in the Sn-C_3N_4 samples closely resemble those of pure C_3N_4, suggesting that the structure of C_3N_4 remains largely unchanged during synthesis. Additionally, the Sn-C_3N_4 nanostructures exhibit a distinct SnO_2 peak at 2θ = 26.6°, associated with the (110) plane of SnO_2 and matching JCPDS No. 01-088-0287, alongside the C_3N_4 peaks, indicating successful incorporation of SnO_2 into the nanostructure [17]. The lack of significant differences between the diffraction patterns of C_3N_4 and Sn-C_3N_4 suggests that the addition of SnO_2 did not alter the overall crystal structure of C_3N_4, confirming that SnO_2 QDs were effectively integrated into the C_3N_4 matrix to form the desired nanocomposite materials. Furthermore, the presence of SnO_2 QDs in the nanostructure was confirmed by HRTEM mapping.

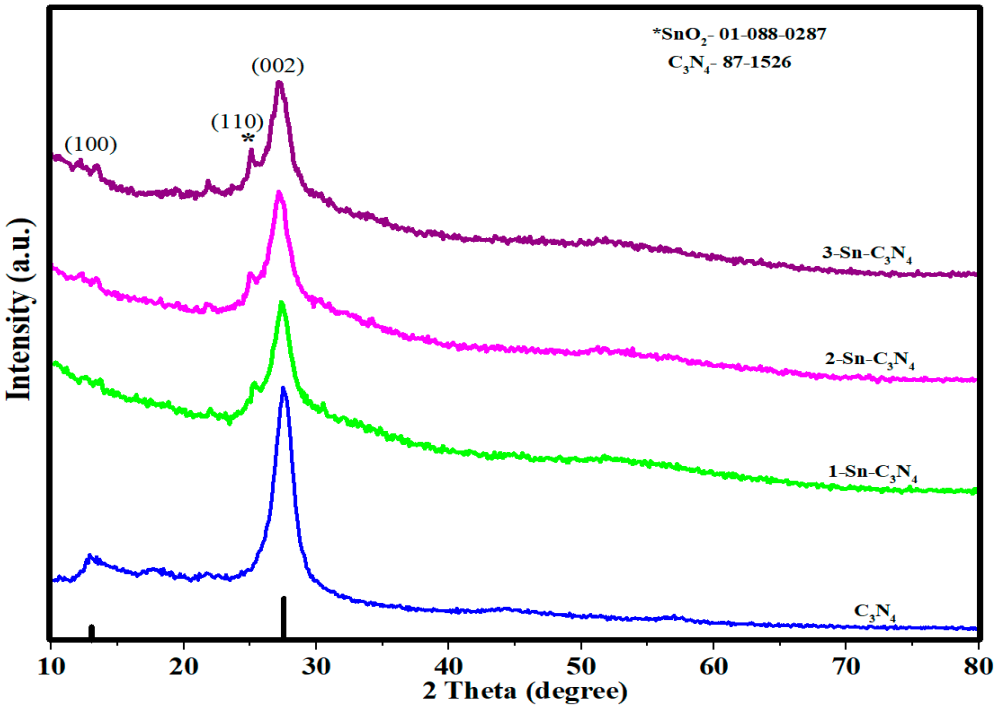

Figure 1. XRD patterns of various photocatalysts: C_3N_4, 1-Sn-C_3N_4, 2-Sn-C_3N_4, and 3-Sn-C_3N_4.

Figure 2 presents the FTIR spectra of the C_3N_4, 1-Sn-C_3N_4, 2-Sn-C_3N_4, and 3-Sn-C_3N_4 photocatalysts, highlighting their critical structural features. The characteristic peak of pristine C_3N_4 was detected at 805 cm^{-1}, which can be attributed to the breathing mode of triazine rings, a hallmark of the basic C_3N_4 framework. The peaks within the 1200–1650 cm^{-1} range are associated with C-N stretching vibrations from the aromatic loops, likely originating from the C≡N stretching modes in conjugated systems [18]. Moreover, the broad peak in the 3000–3400 cm^{-1} region is typically attributed to the stretching vibrational modes of -NH groups and surface-adsorbed H_2O molecules. For the SnO_2 QD-decorated C_3N_4 nanostructures (Sn-C_3N_4), no significant shifts in the FTIR peaks were observed, suggesting that the core C_3N_4 structure was preserved after the incorporation of SnO_2 QDs. However, a noticeable decrease in the FTIR peak intensity was evident as SnO_2 QDs were introduced into the C_3N_4 matrix. This reduction in peak intensity suggests interactions between the SnO_2 QDs and the C_3N_4 nanosheets, implying that the presence of SnO_2 QDs influences the surface chemistry of C_3N_4. The weakening of these characteristic peaks may be attributed to the partial coverage of C_3N_4 by SnO_2 QDs, which could reduce the exposure of the functional groups responsible for the FTIR signals. These findings, along with the XRD

results, confirm the successful integration of SnO_2 QDs with C_3N_4, supporting the presence of a strong interaction between the two components in the nanocomposite. This interaction is essential for enhancing the photocatalytic properties of the Sn-C_3N_4 nanostructures, as it likely promotes more efficient charge separation and transfer, thereby improving the overall photocatalytic performance.

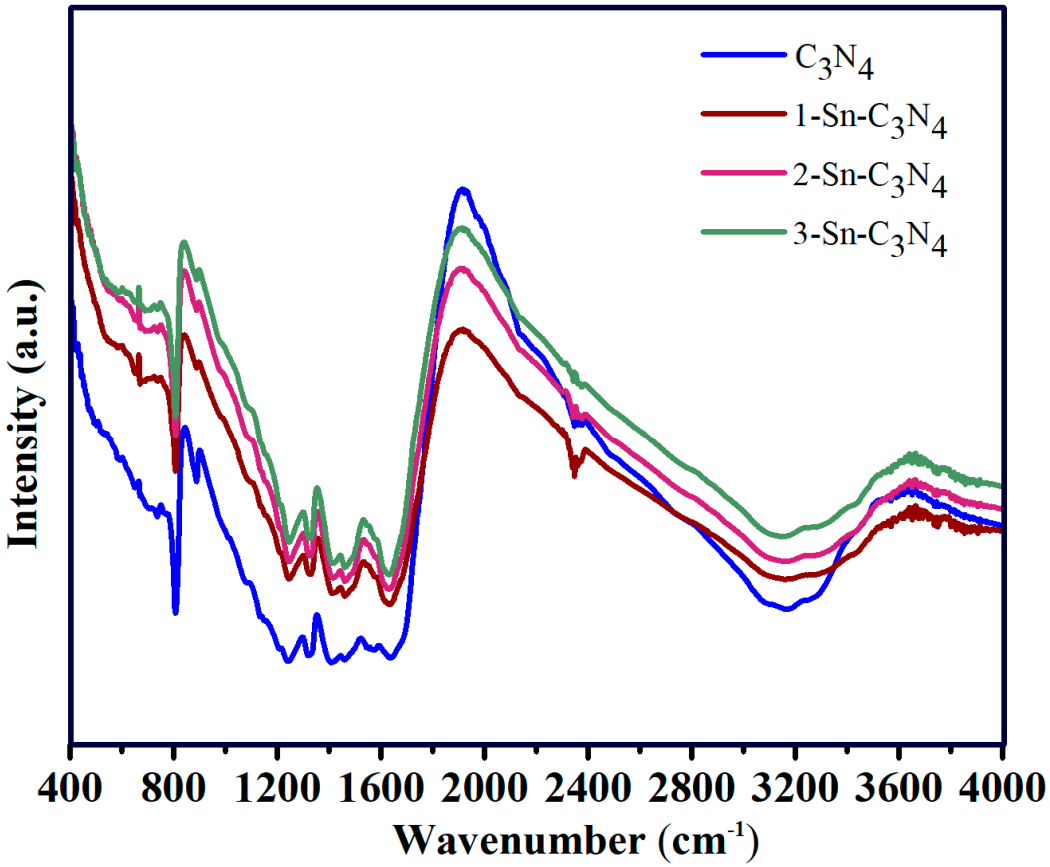

Figure 2. FTIR spectra of various photocatalysts: C_3N_4, 1-Sn-C_3N_4, 2-Sn-C_3N_4, and 3-Sn-C_3N_4.

HRTEM is a powerful technique for examining the structural properties of thin nanosheets. Figure 3a–e shows the HRTEM images of the 3-Sn-C_3N_4 nanostructure, revealing a distinct 2D mesoporous network composed of thin C_3N_4 layers only a few nanometers thick. This structure incorporates quantum-sized SnO_2 nanoparticles, which are not easily distinguishable at lower magnifications. However, these SnO_2 QDs become more apparent in higher-magnification images (Figure 4b). The SAED pattern of the 3-Sn-C_3N_4 nanostructure (Figure 3f) further supports these observations, highlighting the amorphous nature of the C_3N_4 sheets, while the faint diffraction rings correspond to the crystalline SnO_2 QDs. This contrast between the amorphous carbon nitride and crystalline SnO_2 QDs underscores the successful formation of a hybrid nanostructure. Figure 4a presents a HRTEM image of the 3-Sn-C_3N_4 nanostructure, where single-atom SnO_2 QDs (visible as white dots) are randomly distributed across the surface of the C_3N_4 nanosheets. In the higher-magnification TEM images (Figure 4b), the QDs, only a few nanometers in size, are observed to be attached to the surface edges of the C_3N_4. These SnO_2 QDs play a critical role in promoting radical formation during photocatalytic reactions, thereby enhancing the system's overall reactivity. The HAADF image at an 80 nm scale (Figure 4c) further confirms the anchoring of SnO_2 QDs to the C_3N_4's surface. This intimate attachment between the SnO_2 QDs and C_3N_4 nanosheets is essential for enhancing photocatalytic activity by improving charge separation and transfer efficiency. Additionally, Figure 4d displays the combined elemental mapping of the 3-Sn-C_3N_4 nanostructure, while individual element maps for C, N, Sn, and

O provide clear evidence of the uniform distribution of SnO_2 QDs within the C_3N_4 matrix. This uniformity confirms the successful formation of a heterostructure, which is crucial for enhancing photocatalytic reactions by facilitating efficient charge carrier dynamics and increasing the active sites for photocatalytic processes.

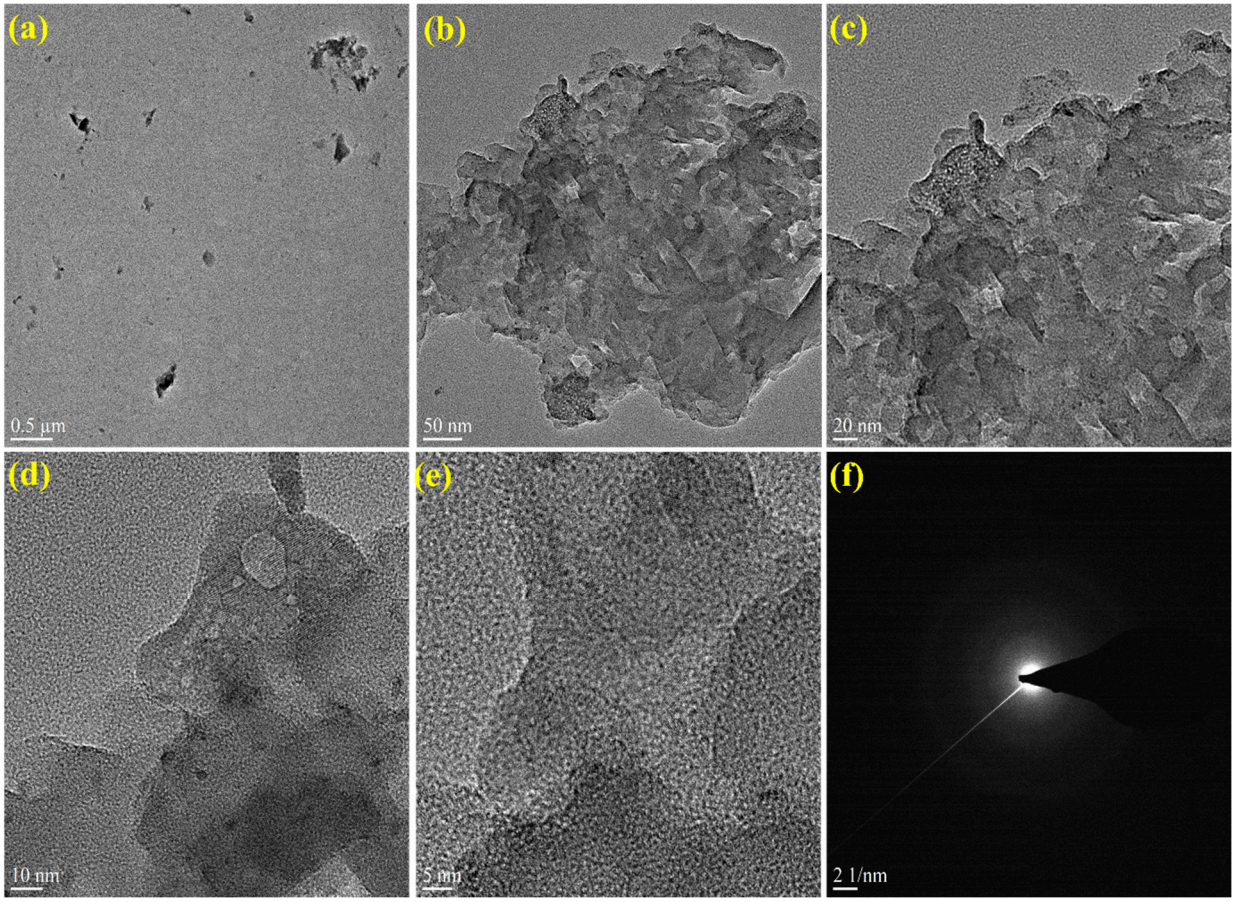

Figure 3. (**a**–**e**) HRTEM images and (**f**) SAED pattern of the 3-Sn-C_3N_4 photocatalyst.

XPS analysis was conducted to investigate the chemical composition of the 3-Sn-C_3N_4 nanostructure. Figure 5a presents the full-scan XPS survey, confirming the successful integration of SnO_2 and C_3N_4 within the composite material. The presence of characteristic peaks for both components indicates that the nanostructure consists of well-defined SnO_2 QDs anchored to the C_3N_4 nanosheets. Figure 5b shows the XPS spectra of C 1s, revealing two prominent deconvoluted peaks. The peak at 284.5 eV corresponds to sp^2-hybridized carbon atoms linked to two N atoms within the aromatic ring structure of C_3N_4. The additional peak at 287.9 eV is attributed to carbon atoms associated with the terminal -NH_2 groups [19], confirming the integrity of the C_3N_4 structure within the composite. The N 1s XPS spectra (Figure 5c) provide further insight into the nitrogen species present in the nanostructure, displaying three distinct peaks at 398.4, 400.3, and 404.1 eV. The peak at 398.4 eV corresponds to the nitrogen atoms attached to three carbon atoms (N-$(C)_3$) within the C_3N_4 framework [20]. The peak at 400.3 eV is attributed to surface amino groups (-NH_2), while the bump at 404.1 eV represents π-excitation within the C/N heterocyclic system. These findings confirm the chemical environment of nitrogen in the C_3N_4 nanosheets and the retention of its structural features upon incorporation of SnO_2. Figure 5d shows the Sn 3d XPS spectra of the 3-Sn-C_3N_4 nanostructure, with characteristic binding energies at 486.6 eV and 494.9 eV corresponding to the Sn $3d_{5/2}$ and Sn $3d_{3/2}$ peaks, respectively. These peaks indicate the presence of Sn^{4+} oxidation states, confirming that Sn exists as

SnO_2 within the nanostructure [21]. The XPS analysis conclusively demonstrates that SnO_2 QDs were effectively combined with C_3N_4, forming a stable composite material.

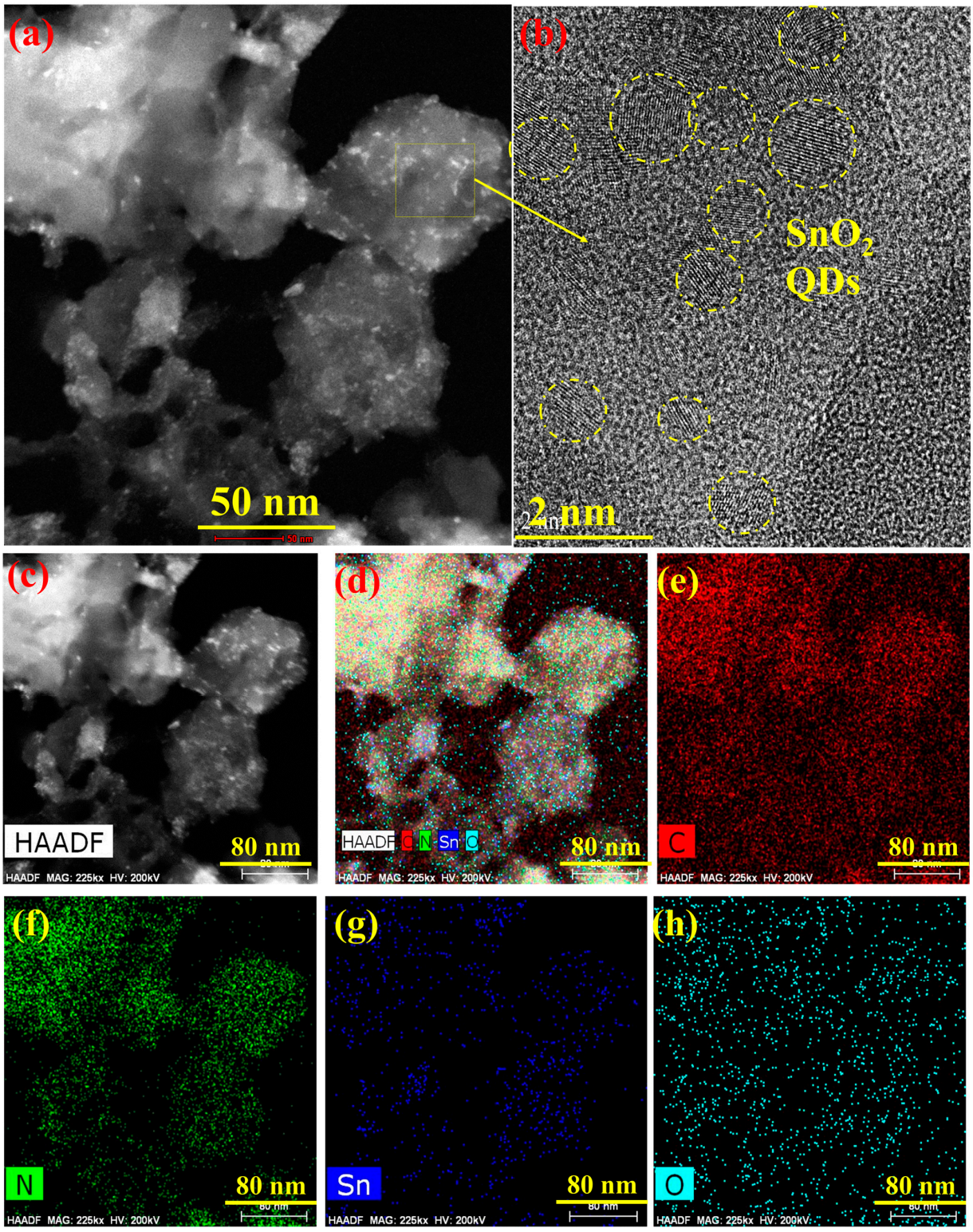

Figure 4. (**a**) STEM image, (**b**) high-magnification TEM image at 2 nm, yellow dotted circle reveals the SnO_2QDs, (**c**) HAADF image, (**d**) combined elemental mapping, and (**e**–**h**) individual element mapping of C, N, Sn, and O for the 3-Sn-C_3N_4 photocatalyst.

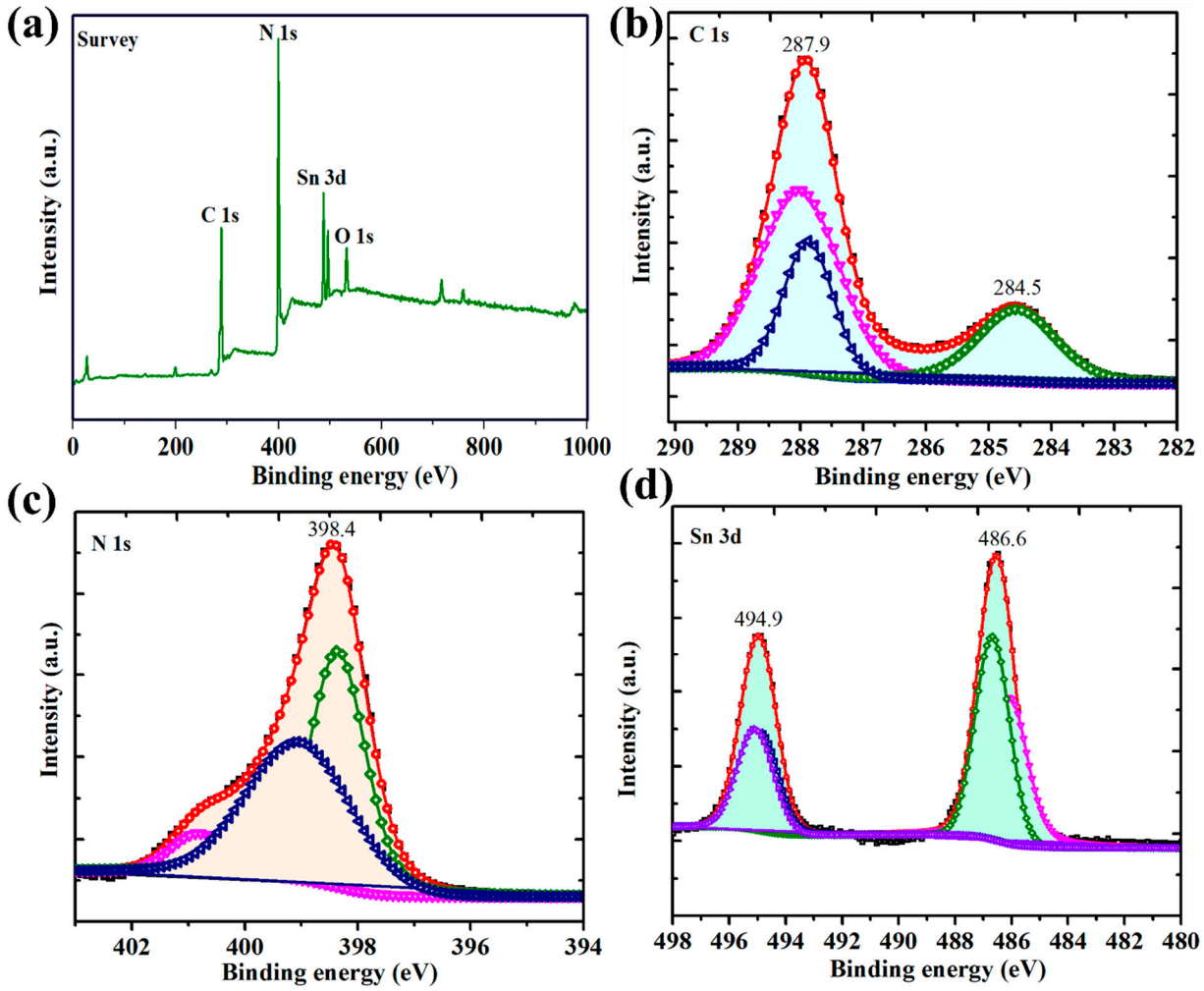

Figure 5. (**a**) Survey scan, (**b**) C1s spectrum, (**c**) N1s spectrum, and (**d**) Sn 3d spectrum of the 3-Sn-C_3N_4 photocatalyst.

UV–vis–NIR absorbance spectroscopy was used to evaluate the light-harvesting capabilities of the C_3N_4, 1-Sn-C_3N_4, 2-Sn-C_3N_4, and 3-Sn-C_3N_4 photocatalysts, as shown in Figure 6a. The C_3N_4 sample displays an absorption edge extending beyond 460 nm, indicating its ability to absorb visible light, which corresponds to its band gap and allows it to utilize visible light for photocatalytic activity. However, the absorption is relatively weak in the longer visible wavelengths, which limits its efficiency. In the SnO_2-modified nanostructured photocatalysts, absorbance peaks were observed within the visible light range (above 420 nm), indicating enhanced light absorption in this region. Compared with bulk C_3N_4, these nanostructured photocatalysts exhibited a broader light absorption capacity, particularly within the visible spectrum. This extended light-harvesting capability is crucial, as it facilitates the generation of additional charge carriers, thereby boosting photocatalytic efficiency. Figure 6b presents the energy band gaps of the C_3N_4, 1-Sn-C_3N_4, 2-Sn-C_3N_4, and 3-Sn-C_3N_4 photocatalysts analyzed by Tauc plots. The calculated band gaps were found to be 2.69 eV for C_3N_4, 2.68 eV for 1-Sn-C_3N_4, 2.65 eV for 2-Sn-C_3N_4, and 2.62 eV for 3-Sn-C_3N_4.

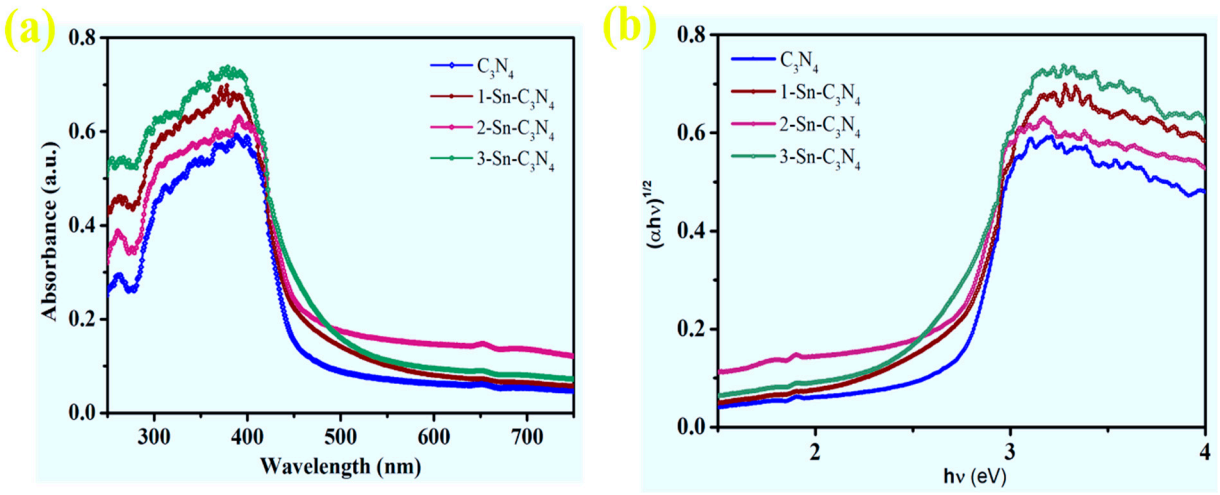

Figure 6. (**a**) UV–vis absorbance spectra and (**b**) Tauc plots of the C_3N_4, 1-Sn-C_3N_4, 2-Sn-C_3N_4, and 3-Sn-C_3N_4 photocatalysts.

The surface area and mesoporous characteristics of the C_3N_4 and 3-Sn-C_3N_4 nanostructures were examined using N_2 adsorption–desorption loops, as shown in Figure 7a. The observed isotherms exhibit H3-type hysteresis loops, indicating the presence of mesoporous structures within the photocatalysts [22]. The BET surface areas of the C_3N_4 and 3-Sn-C_3N_4 nanostructures were measured to be 8.04 m^2/g and 3.96 m^2/g, respectively, demonstrating that the inclusion of SnO_2 QDs significantly increases the surface area of the nanostructures. Additionally, the BJH pore-size distribution curves (Figure 7b) show that the average pore sizes for the C_3N_4 and 3-Sn-C_3N_4 nanostructures are 21.85 nm and 34.75 nm, respectively. This increase in pore size for the SnO_2-modified structure further supports its mesoporous nature. The larger surface area and enhanced pore size in the 3-Sn-C_3N_4 nanostructure, attributed to the quantum effects of SnO_2, are advantageous for improving photocatalytic performance. The increased surface area provides more active sites for photocatalytic reactions, while the mesoporous structure enhances mass transport and light penetration, both of which contribute to the higher photoactivity of the Sn-C_3N_4 nanostructures compared with pure C_3N_4. This enhancement is particularly beneficial for applications such as pollutant degradation and H_2 generation.

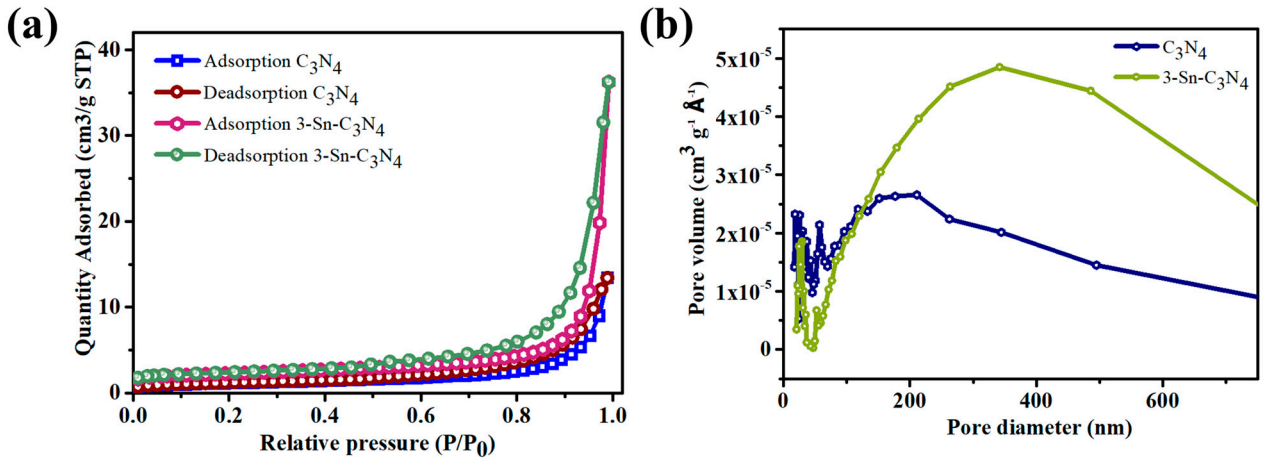

Figure 7. (**a**) N_2 adsorption–desorption isotherms and (**b**) pore size distribution of the C_3N_4 and 3-Sn-C_3N_4 photocatalysts.

The photodegradation efficiency of C_3N_4, 1-Sn-C_3N_4, 2-Sn-C_3N_4, and 3-Sn-C_3N_4 photocatalysts was evaluated by examining the degradation of CV dye in aqueous solutions.

Figure 8a–d show the UV–visible absorption spectra of CV dye over time for each photocatalyst. Before photocatalytic testing, the photocatalysts were suspended in the dye solution and kept in the dark for 30 min at room temperature with stirring to establish adsorption–desorption equilibrium. Among the tested photocatalysts, 3-Sn-C_3N_4 demonstrated the highest photocatalytic activity for CV dye degradation compared with the other samples, including bare C_3N_4. This enhanced performance can be attributed to the larger surface area of 3-Sn-C_3N_4 (8.04 m^2/g), which enables a higher dye adsorption capacity than C_3N_4 (3.96 m^2/g) (Figure 9a). A larger surface area facilitates greater dye adsorption, which, in turn, enhances photoactivity by increasing the number of active sites available for the reaction.

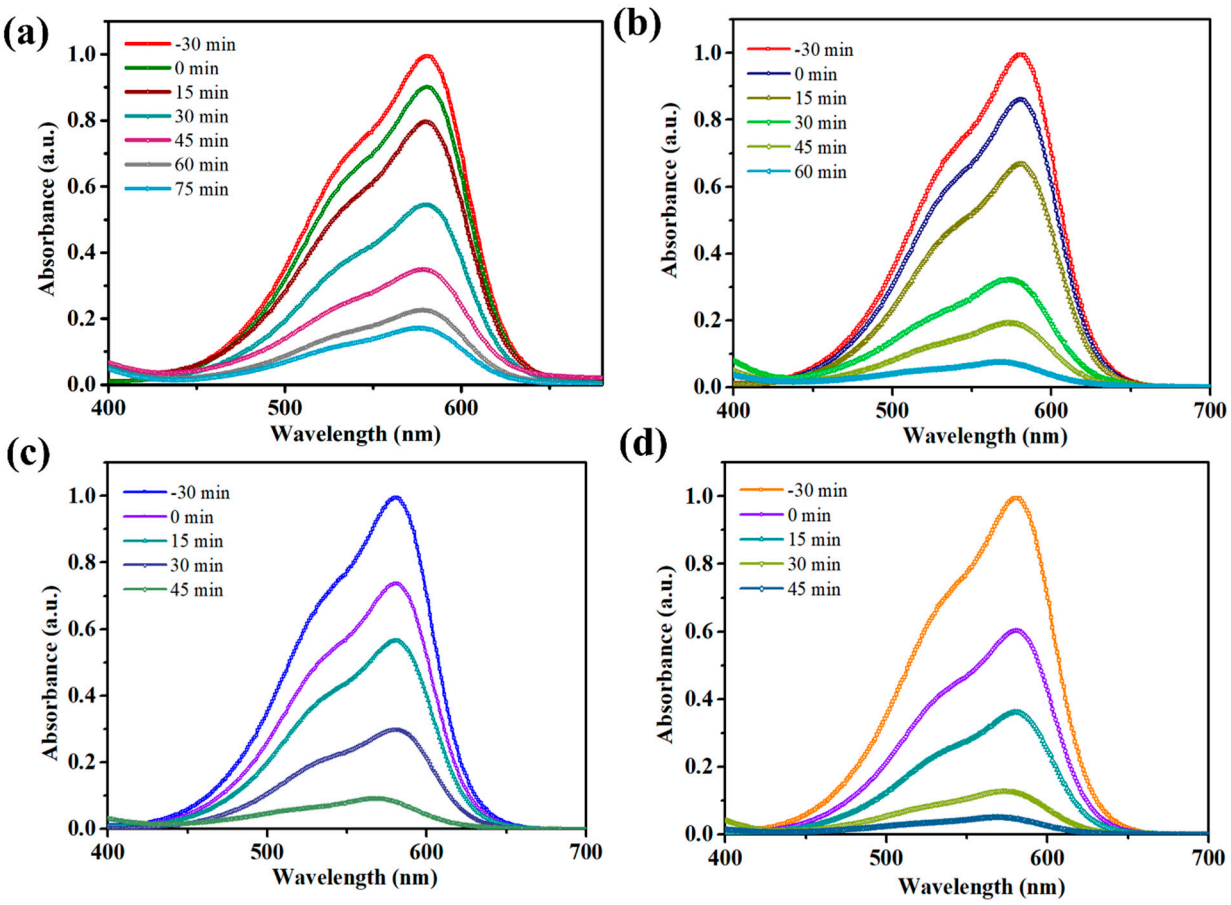

Figure 8. UV–vis absorbance spectra of CV dye degradation of the (**a**) C_3N_4, (**b**) 1-Sn-C_3N_4, (**c**) 2-Sn-C_3N_4, and (**d**) 3-Sn-C_3N_4 photocatalysts.

The reaction kinetics for CV dye degradation were analyzed using the logarithmic relationship $\ln(C/C_0)$ to further compare the photocatalytic efficiency (Figure 9b). The rate constants for the C_3N_4 and 3-Sn-C_3N_4 photocatalysts were determined to be 0.002/min and 0.0052/min, respectively. The significantly higher rate constant for 3-Sn-C_3N_4 can be attributed to its increased surface area and enhanced light absorption capacity, both resulting from the inclusion of SnO_2 QDs. This phenomenon facilitates more efficient charge separation and transfer during the photocatalytic process. The reusability of the 3-Sn-C_3N_4 nanostructure was also evaluated through four consecutive cycles of CV dye degradation (Figure 10a). The results indicate no notable decrease in photocatalytic activity after multiple uses, confirming the stability and durability of the 3-Sn-C_3N_4 photocatalyst. Moreover, a comparison of the photocatalytic performance across various photocatalysts demonstrated that the inclusion of SnO_2 QDs significantly enhances the photocatalytic activity of C_3N_4 through synergistic and plasmonic effects, resulting in more effective CV

dye degradation. This improvement highlights the potential of SnO_2-QD-modified C_3N_4 as an effective photocatalyst for environmental pollutant removal.

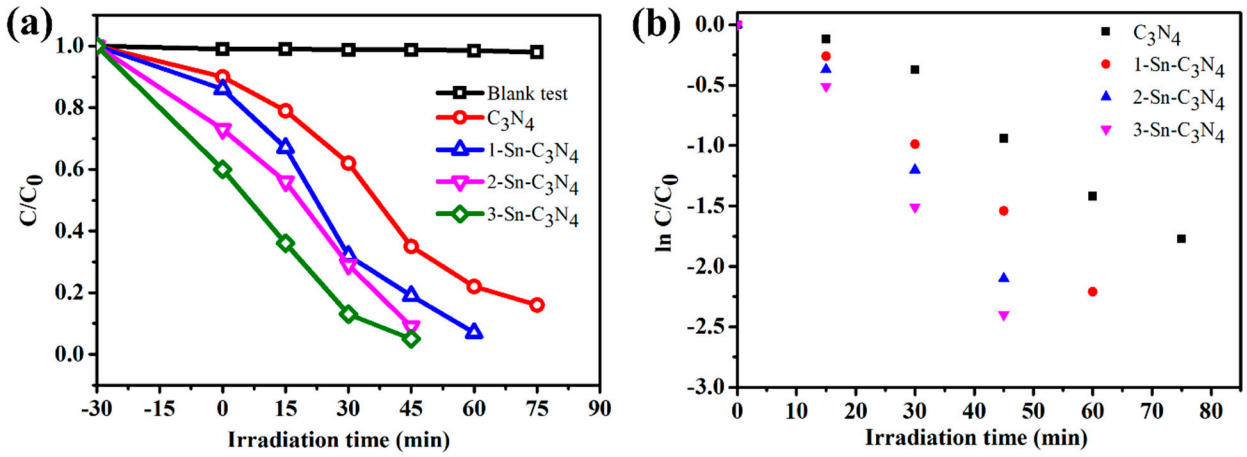

Figure 9. (**a**) Photocatalytic activity and (**b**) kinetic linear simulations for CV dye degradation by the C_3N_4, 1-Sn-C_3N_4, 2-Sn-C_3N_4, and 3-Sn-C_3N_4 photocatalysts.

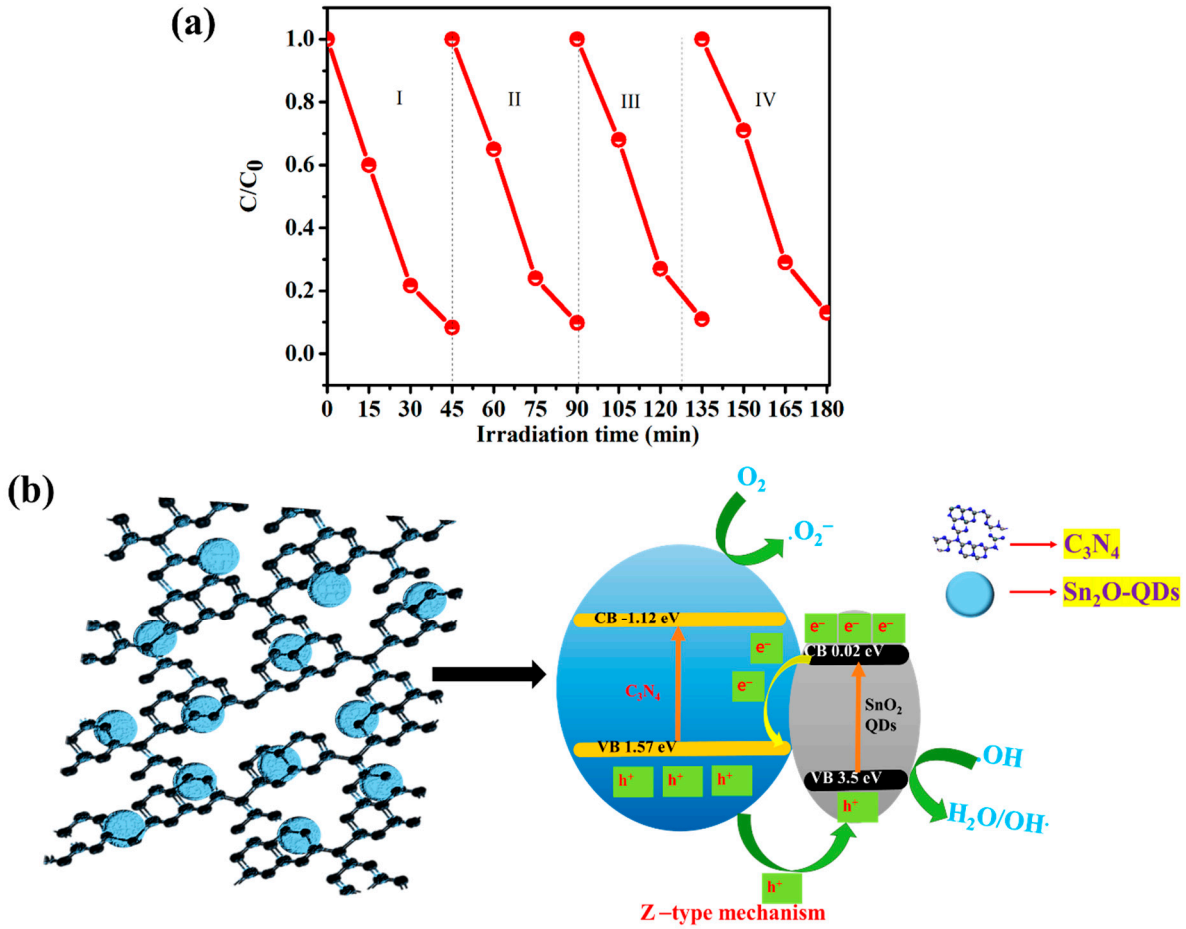

Figure 10. (**a**) Cycling stability of the 3-Sn-C_3N_4 photocatalyst and (**b**) proposed photocatalytic mechanism of the 3-Sn-C_3N_4 photocatalyst.

Under solar light irradiation, the formation of $O_2^{\bullet-}$ is hindered because the CB potential of SnO_2 QDs is 0.1 eV, which is more positive than the redox potential of $O_2/O_2^{\bullet-}$ (−0.33 eV) [23,24]. Despite this, previous studies have shown that $O_2^{\bullet-}$ is a key reactive

species driving the photocatalytic process in such nanostructure systems [23]. Consequently, a Z-scheme mechanism is proposed to best match our experimental observations (Figure 10b). Upon irradiation, electrons generated in the conduction band of SnO_2 QDs transfer to the VB of C_3N_4, and from there, these electrons migrate to the CB of C_3N_4. At this point, they interact with O_2 molecules, generating $O_2^{\bullet-}$, the primary active species responsible for dye degradation. Concurrently, holes remain in the VB of SnO_2 QDs, where they contribute to the oxidation of H_2O, producing •OH radicals that further enhance the photocatalytic process. This Z-scheme mechanism not only facilitates the effective separation of photoinduced charge carriers, reducing recombination, but also preserves the strong redox potential within the nanostructure. This leads to improved photocatalytic efficiency, as both $O_2^{\bullet-}$ and •OH radicals serve as potent oxidants that decompose dye molecules, driving the degradation process. This mechanism highlights the synergistic interaction between SnO_2 QDs and C_3N_4 that is crucial to enhancing photocatalytic performance. The possible reactions involved in the photocatalytic degradation of CV dyes by SnO_2 QDs-C_3N_4 nanostructures are as follows:

$$SnO_2\ QDs\text{-}C_3N_4 \rightarrow SnO_2\ QDs\text{-}C_3N_4\ (h_{VB}^{+} + e_{CB}^{-}) \quad (1)$$

$$C_3N_4\ (e_{CB}^{-}) + SnO_2\ QDs \rightarrow SnO_2\ QDs\ (e_{CB}^{-}) + C_3N_4 \quad (2)$$

$$e_{CB}^{-} + O_2 \rightarrow O_2^{\bullet-} \quad (3)$$

$$O_2^{\bullet-} + \text{CV dye} \rightarrow \text{Degraded products} \quad (4)$$

$$\bullet OH + \text{CV dye} \rightarrow \text{Degraded products} \quad (5)$$

The photocatalytic H_2 evolution efficiency of the synthesized nanostructured photocatalysts—the C_3N_4, 1-Sn-C_3N_4, 2-Sn-C_3N_4, and 3-Sn-C_3N_4 photocatalysts—was systematically evaluated, using TEOA as the sacrificial agent to promote H_2 generation. As shown in Figure 11a,b, the H_2 yields from C_3N_4, 1-Sn-C_3N_4, 2-Sn-C_3N_4, and 3-Sn-C_3N_4 were measured at 281, 1187.3, 1254.6, and 1305.4 μmol/h/g, respectively. Remarkably, the incorporation of SnO_2 QDs into the C_3N_4 matrix led to a substantial increase in H_2 yield, reaching up to 4.64 times that of pure C_3N_4. This significant improvement in photocatalytic efficiency is attributed to the presence of SnO_2 QDs, which enhance the separation and capture of photoinduced charge carriers, thereby reducing electron–hole recombination.

Figure 11c shows the impact of various scavengers on the photocatalytic H_2 yield using the 3-Sn-C_3N_4 nanostructure. Among the tested scavengers, TEOA produced the highest H_2 yield, confirming its effectiveness in enhancing photocatalytic activity. Consequently, TEOA was chosen as the model scavenger for this study. The stability and reusability of the 3-Sn-C_3N_4 photocatalyst were further assessed over three consecutive H_2 evolution cycles under identical photocatalytic conditions (Figure 11d). After the third cycle, the H_2 production rate decreased slightly to 1214 μmol/h/g, suggesting minimal degradation in performance. This stability demonstrates that the 3-Sn-C_3N_4 photocatalyst is highly robust for repeated use, benefiting from the synergistic interaction between SnO_2 QDs and C_3N_4. Enhanced interfacial charge transfer between SnO_2 QDs and C_3N_4 plays a vital role in maintaining efficient photocatalytic H_2 generation over multiple cycles.

To better understand the charge carrier transport behavior of the photocatalysts, photocurrent response measurements were performed for C_3N_4 and 3-Sn-C_3N_4 under light irradiation in a 0.5 M Na_2SO_4 solution (Figure 12a). The 3-Sn-C_3N_4 photocatalyst demonstrated a significantly higher photocurrent density of 0.068 μA cm^2, compared with 0.033 μA cm^2 for the C_3N_4 photocatalyst. This evaluated photocurrent response indicates that 3-Sn-C_3N_4 achieves more efficient electron–hole pair separation, reducing recombination and thus enhancing the photocatalytic performance. Additionally, EIS analysis was conducted to investigate the charge transfer properties of both photocatalysts, with the Nyquist plots shown in Figure 12b. A smaller semicircle in the Nyquist plot typically reflects improved interfacial charge mobility. Here, 3-Sn-C_3N_4 displayed a noticeably smaller semicircle than C_3N_4, indicating superior charge transfer across the photocatalyst

interface. These results suggest that the 3-Sn-C_3N_4 nanostructure provides enhanced interfacial charge migration and a lower recombination rate, likely due to the strong interaction and close integration between SnO_2 QDs and C_3N_4. This synergy promotes more efficient photocatalytic processes.

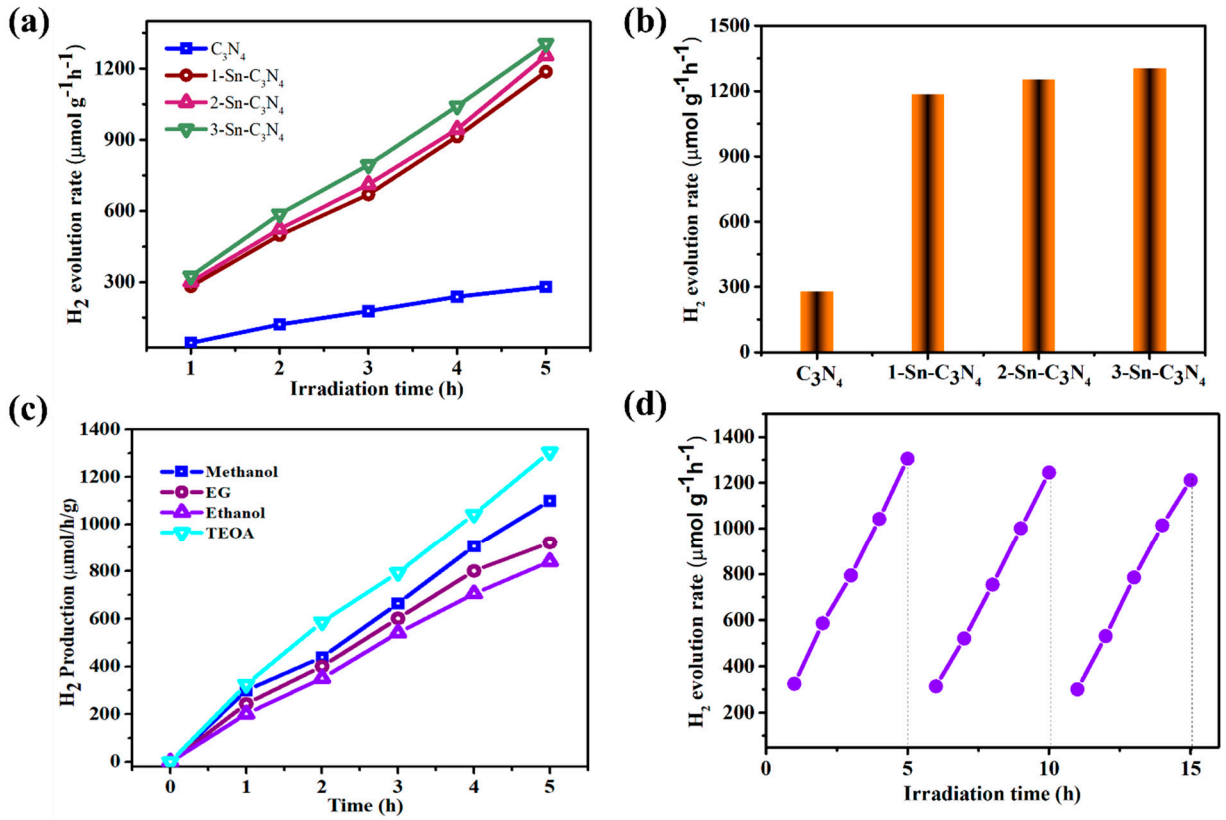

Figure 11. (**a**) Photocatalytic H_2 production; (**b**) comparision of H_2 production among the C_3N_4, 1-Sn-C_3N_4, 2-Sn-C_3N_4, and 3-Sn-C_3N_4 photocatalysts; (**c**) effect of different scavengers on the 3-Sn-C_3N_4 photocatalyst; and (**d**) continuous cycling results for the 3-Sn-C_3N_4 photocatalyst.

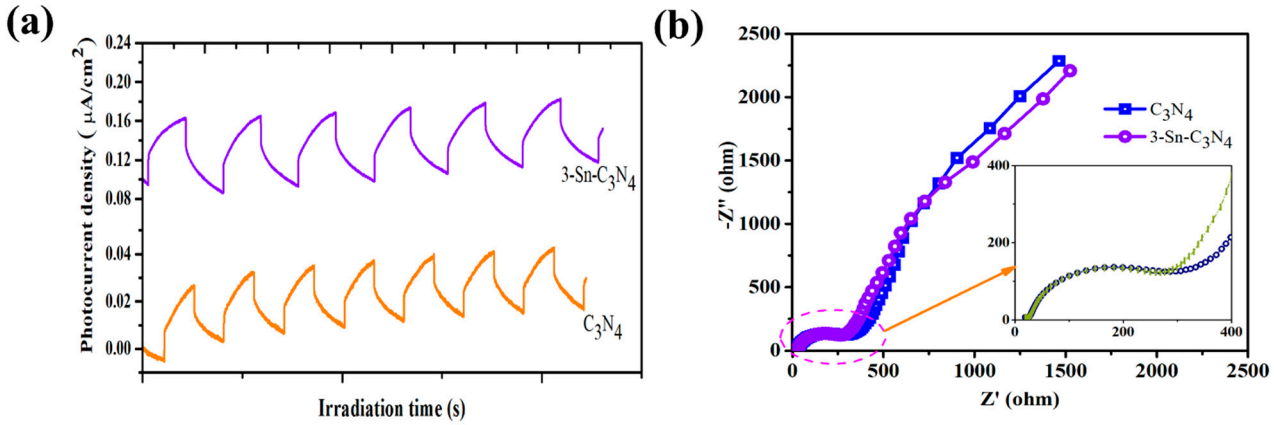

Figure 12. (**a**) Transient photocurrent density of the C_3N_4 and 3-Sn-C_3N_4 photocatalysts in a 0.5 M Na_2SO_4 electrolyte, and (**b**) EIS spectra for the C_3N_4 and 3-Sn-C_3N_4 photocatalysts.

The exceptional performance of the 3-Sn-C_3N_4 nanostructure can be attributed to several key factors. The heterostructure formed between C_3N_4 and SnO_2 QDs facilitates efficient charge separation by reducing electron–hole recombination, a common limitation in pure C_3N_4 systems. This improved charge separation extends the lifetime of reactive species, including hydroxyl radicals and superoxide anions, which play crucial roles in degrading organic dye molecules. Additionally, the incorporation of SnO_2 QDs increases the number of active sites on the nanocomposite's surface, enhancing interactions with dye molecules and accelerating their breakdown. The synergistic interaction between C_3N_4 and SnO_2 QDs not only boosts their overall photocatalytic efficiency but also highlights the potential of these composites to overcome the limitations of traditional photocatalysts, presenting a promising solution for environmental applications.

3. Materials and Methods

Synthesis of SnO_2 QDs/C_3N_4 Nanostructures

For this, 7 g of melamine was mixed with varying amounts of anhydrous tin chloride (0.9, 0.95, and 1 g) using an agate mortar to ensure a uniform mixture. The mixtures were then transferred into a ceramic crucible and subjected to heat treatment at 530 °C for 12 h. The samples were cooled to 25 °C after the reaction, and the resulting precipitates were thoroughly washed multiple times with H_2O and ethanol to remove any impurities. The cleaned products were then dried at 100 °C to yield the final nanostructures. The samples were labeled as 1-Sn-C_3N_4, 2-Sn-C_3N_4, and 3-Sn-C_3N_4, corresponding to the different concentrations of tin precursor used. A detailed characterization of the synthesized nanostructures, including photocatalytic and electrochemical performance tests, is provided in the Supplementary Materials. These tests were conducted to evaluate the efficiency of the SnO_2 QD-C_3N_4 composites in photocatalytic degradation and H_2 evolution, as well as to analyze the charge transfer dynamics.

4. Conclusions

In summary, this study successfully developed SnO_2 QDs-C_3N_4 nanostructures based on a single-step pyrolysis method, achieving significant enhancements in photocatalytic activity for CV dye degradation and H_2 production under solar light. The 3-Sn-C_3N_4 nanostructure exhibited a notably higher H_2 evolution rate (1305.4 μmol/h/g) compared with bare C_3N_4 (281 μmol/h/g). The unique 0D/2D architecture of the Sn-C_3N_4 nanocomposites, incorporating SnO_2 QDs, increased the surface area and enabled efficient charge separation between SnO_2 and C_3N_4. This expanded surface area, combined with improved charge separation and enhanced light absorption, contributed to its outstanding photocatalytic performance. Electrochemical studies, including photocurrent responses and impedance spectroscopy, further validated the efficient charge transport and reduced recombination rates in the 3-Sn-C_3N_4 structure. Additionally, the nanostructure demonstrated strong photostability and reusability, making it a promising candidate for applications in environmental and energy. This work offers an effective strategy for designing advanced photocatalysts with enhanced light utilization and charge carrier dynamics, paving the way for future innovations in photocatalytic materials.

Supplementary Materials: The following supporting information can be downloaded at https://www.mdpi.com/article/10.3390/catal14110824/s1. Characterization and photocatalytic test procedures.

Author Contributions: Conceptualization: S.V.P.V.; methodology, S.V.P.V. and H.P.K.S.; formal analysis, P.R.; data curation, S.V.P.V.; writing—original draft preparation, M.A.H.; writing—review and editing, M.A.H. and J.S.; funding acquisition, M.A.H. and J.S. All authors have read and agreed to the published version of the manuscript.

Funding: This work was funded by the Researchers' Supporting Project Number (RSP2024R441) at King Saud University, Riyadh, Saudi Arabia, and this work was also supported by the National Research Foundation of Korea (NRF) grant funded by the Korean government (MSIT) (No. RS-2023-00280665).

Data Availability Statement: All data supporting the findings of this study are available within the paper and its Supplementary Materials published online.

Conflicts of Interest: The authors declare no conflict of interest.

References

1. Ahmed, M.A.; Mahmoudb, S.A.; Mohamed, A.A. Unveiling the photocatalytic potential of graphitic carbon nitride (g-C_3N_4): A state-of-the-art review. *RSC Adv.* **2024**, *14*, 25629–25662. [CrossRef] [PubMed]
2. Kyriakos, P.; Hristoforou, E.; Belessiotis, G.V. Graphitic Carbon Nitride (g-C_3N_4) in Photocatalytic Hydrogen Production: Critical Overview and Recent Advances. *Energies* **2024**, *17*, 3159. [CrossRef]
3. Yin, H.; He, J.; Xiao, B.; Zhou, M.; Wang, W.; Cunha, J.; Chen, Z.; Hou, Z.; Zhang, T.; Yu, Z. Advances and prospects of g-C_3N_4 in lithium-sulfur batteries. *Nano Res. Energy* **2024**. [CrossRef]
4. Yu, Z.; Li, Y.; Torres-Pinto, A.; LaGrow, A.P.; Diaconescu, V.M.; Simonelli, L.; Sampaio, M.J.; Bondarchuk, O.; Amorim, I.; Araujo, A.; et al. Single-atom Ir and Ru anchored on graphitic carbon nitride for efficient and stable electrocatalytic/photocatalytic hydrogen evolution. *Appl. Catal. B Environ.* **2022**, *310*, 121318. [CrossRef]
5. Weldekirstos, H.D.; Mengist, T.; Belachew, N.; Mekonnen, M.L. Enhanced photocatalytic degradation of methylene blue dye using fascily synthesized g-C_3N_4/$CoFe_2O_4$ composite under sun light irradiation. *Results Chem.* **2024**, *7*, 101306. [CrossRef]
6. Mittal, S.; Khosya, M.; Singh, M.; Khare, N. 2D/2D heterojunction of SnS_2/g-C_3N_4 nanocomposite photoelectrode for improved photoelectrochemical water splitting performance. *Appl. Surf. Sci.* **2024**, *677*, 161016. [CrossRef]
7. Song, X.-L.; Chen, L.; Gao, L.-J.; Ren, J.-T.; Yuan, Z.-Y. Engineering g-C_3N_4 based materials for advanced photocatalysis: Recent advances. *Green Energy Environ.* **2024**, *9*, 166–197. [CrossRef]
8. Fareed, I.; Farooq, M.U.H.; Khan, M.D.; Tahir, M.; Butt, F.K. An efficient multifunctional SnS_2/g-C_3N_4 hierarchical nanoflower catalyst for electrocatalytic and photocatalytic applications. *Ceram. Int.* **2024**, *50*, 36004–36017. [CrossRef]
9. Alsalme, A.; Hesham, M.; Soltan, A.; Mohammed, N.N.; Nejm, A.Q.; Messih, M.F.A.; Hussein, I.A.; Ahmed, M.A. Pioneering the design of S-scheme SnS_2/g-C_3N_4 nanocomposites via sonochemical and physical mixing methods for solar degradation of cationic rhodamine B dye. *Mater. Adv.* **2024**, *5*, 7278–7295. [CrossRef]
10. Lu, J.; Chen, Z.; Shen, Y.; Yuan, H.; Sun, X.; Hou, J.; Guo, F.; Li, C.; Shi, W. Boosting photothermal-assisted photocatalytic H_2 production over black g-C_3N_4 nanosheet photocatalyst via incorporation with carbon dots. *J. Colloid Interface Sci.* **2024**, *670*, 428–438. [CrossRef]
11. Zou, Y.; Xie, Y.; Yu, S.; Chen, L.; Cui, W.; Dong, F.; Zhou, Y. SnO_2 quantum dots anchored on g-C_3N_4 for enhanced visible-light photocatalytic removal of NO and toxic NO_2 inhibition. *Appl. Surf. Sci.* **2019**, *496*, 143630. [CrossRef]
12. Ravichandran, K.; Shalini, R.; Kavitha, P.; Praseetha, P.K.; Sriram, S.; Viji, A.; Sivaranjani, V. Earthworm excrete derived-enzyme enriched SnO_2/g-C_3N_4nanocomposite for near complete decomposition of toxic dye molecules. *Mater. Chem. Phys.* **2024**, *320*, 129445. [CrossRef]
13. Bhattacharjee, B.; Hazarika, B.; Ahmaruzzaman, M. Visible-light-driven photocatalytic degradation of Rose Bengal and Methylene Blue using low-cost sawdust derived SnO_2 QDs@g-C_3N_4/biochar nanocomposite. *Environ. Sci. Pollut. Res.* **2023**, *30*, 112591–112610. [CrossRef] [PubMed]
14. Khan, S.S.; Steffy, J.P.; Sruthi, L.; Syed, A.; Elgorban, A.M.; Abid, I.; Wong, L.S. Construction of ZnS QDs decorated gC_3N_4 nanosheets for enhanced catalytic degradation of Rhodamine B. *Ceram. Int.* **2024**, *50*, 36479–36486. [CrossRef]
15. Li, S.; Tan, J.; Liu, J.; Li, Y.; Sun, L.; Huang, Z.; Li, J. Recent Research Progress on Surface Modified Graphite Carbon Nitride Nanocomposites and Their Photocatalytic Applications: An Overview. *Catalysts* **2024**, *14*, 636. [CrossRef]
16. Zhou, Y.; Cai, J.; Sun, Y.; Jia, S.; Liu, Z.; Tang, X.; Hu, B.; Zhang, Y.; Yan, Y.; Zhu, Z. Research on Cu-Site Modification of g-C_3N_4/CeO_2-like Z-Scheme Heterojunction for Enhancing CO_2 Reduction and Mechanism Insight. *Catalysts* **2024**, *14*, 546. [CrossRef]
17. Javed, M.; Iqbal, S.; Qamar, M.A.; Shariq, M.; Ahmed, I.A.; BaQais, A.; Alzahrani, H.; Ali, S.K.; Masmali, N.A.; Althagafi, T.M.; et al. Fabrication of Effective Co-SnO_2/SGCN Photocatalysts for the Removal of Organic Pollutants and Pathogen Inactivation. *Crystals* **2023**, *13*, 163. [CrossRef]
18. Pareek, S.; Sharma, M.; Lal, S.; Quamara, J.K. Polymeric graphitic carbon nitride–barium titanate nanocomposites with different content ratios: A comparative investigation on dielectric and optical properties. *J. Mater. Sci. Mater. Electron.* **2018**, *29*, 13043–13051. [CrossRef]
19. Zhao, Y.; Shai, X.; Zhou, Q.; Shen, K. Construction of a novel Mott-Schottky heterostructure gas sensor g-C_3N_4/SnO_2 with layered nanorods array for high-sensitivity acetone detection. *Appl. Surf. Sci.* **2025**, *680*, 161333. [CrossRef]
20. Wang, Q.; Chen, X.; Tian, J.; Wei, L.; Liu, Y.; Yang, C. The preparation of S-SnO_2/g-C_3N_4 heterojunction and its photocatalytic degradation of phenol and trichlorophenol. *J. Mater. Sci. Mater. Electron.* **2020**, *31*, 16991–17002. [CrossRef]
21. Salunkhe, T.T.; Bathula, B.; Gurugubelli, T.R.; Pammi, S.V.N.; Yoo, K. Highly efficient Z scheme heterojunction of colloidal SnO_2 quantum dots grafted g-C_3N_4 for the degradation of rhodamine B under visible light. *Results Phys.* **2024**, *62*, 107826. [CrossRef]
22. Ismael, M. Construction of novel Ru-embedded bulk g-C_3N_4 photocatalysts toward efficient and sustainable photocatalytic hydrogen production. *Diam. Relat. Mater.* **2024**, *144*, 111024. [CrossRef]

23. He, Y.; Zhang, L.; Fan, M.; Wang, X.; Walbridge, L.M.; Nong, Q.; Wu, Y.; Zhao, L. Z-scheme SnO_{2-x}/g-C_3N_4 composite as an efficient photocatalyst for dye degradation and photocatalytic CO_2 reduction. *Sol. Energy Mater. Sol. Cells* **2015**, *137*, 175–184. [CrossRef]
24. Qi, K.; Zada, A.; Yang, Y.; Chen, Q.; Khataee, A. Design of 2D–2D NiO/g-C_3N_4 heterojunction photocatalysts for degradation of an emerging pollutant. *Res. Chem. Intermed.* **2020**, *46*, 5281–5295. [CrossRef]